KEK Preprint 2014-35
November 2014
H

A Multi-MW Proton/Electron Linac at KEK

R. BELUSEVIC

IPNS, *High Energy Accelerator Research Organization* (KEK)
1-1 *Oho, Tsukuba, Ibaraki* 305-0801, *Japan*
belusev@post.kek.jp

Contents

Abstract : The main 'bottleneck' limiting the beam power in circular machines is caused by space charge effects that produce beam instabilities. To increase maximally the beam power of a 'proton driver', it is proposed to build a facility consisting solely of a 2.5 GeV injector linac (PI) and a 20 GeV pulsed superconducting linac (SCL). Such a facility could be constructed using the existing KEK accelerator infrastructure. The PI, based on the *European Spallation Source* (ESS) linac, would serve both as an injector to the SCL and a source of proton beams that could be used to copiously produce, e.g., neutrons and muons. Protons accelerated by the SCL would be transferred through the KEK Tristan ring in order to create neutrino, kaon and muon beams for fixed-target experiments. At a later stage, a 70 GeV proton synchrotron could be installed inside the Tristan ring. The SCL, comprising 1.3 GHz ILC-type rf cavities, could also accelerate polarized or unpolarized electron beams. After acceleration, electrons could be used to produce polarized positrons, or may traverse an XFEL undulator.

1 Introduction

The *Standard Model* (SM) of particle physics gives a coherent quantum-mechanical description of electromagnetic, weak and strong interactions based on fundamental constituents — quarks and leptons — interacting via force carriers — photons, W and Z bosons, and gluons. The SM is supported by two theoretical 'pillars': the *gauge principle* and the *Higgs mechanism* for particle mass generation. Whereas the gauge principle has been firmly established through precision electroweak measurements, the Higgs mechanism is yet to be fully tested.

Preliminary results on searches for a SM Higgs boson were presented in 2012 by the ATLAS and CMS collaborations at the CERN *Large Hadron Collider* (LHC) [1, 2]. A state decaying to several distinct final states had been observed with a statistical significance of five standard deviations. The observed state has a mass of about 125 GeV. Its production rate is consistent with the predicted rate for the SM Higgs boson. Event yields in different production topologies and different decay modes are self-consistent [3].

To discover a new particle (such as the Higgs boson), or to search for physics beyond the SM, usually requires the use of high-energy hadron or electron-positron colliders. However, many important discoveries in particle physics have been made using proton beams with relatively low energies but high intensities (flavor mixing in quarks and in neutrinos are noteworthy examples). Experiments with high-intensity neutrino beams, e.g., are designed primarily to explore the mass spectrum of the neutrinos and their properties under the CP symmetry.

Some of the most important discoveries emerged from high-precision studies of K mesons ('kaons'), in particular *neutral kaons*. A deeper insight into CP violation is expected to be gained from measurements of ultra-rare kaon decays such as $K^0_{\rm L} \to \pi^0\nu\bar{\nu}$ and $K^+_{\rm L} \to \pi^+\nu\bar{\nu}$. These decays provide important information on higher-order effects in electroweak interactions, and therefore can serve as a probe of new phenomena not predicted by the Standard Model.

The physics programs briefly described in this note are, to a large extent, complementary to each other. For instance, neutrino oscillation experiments and searches for permanent electric dipole moments both look for new sources of CP violation, a phenomenon which reflects the fundamental difference between matter and antimatter.

A unique feature of the proposed facility is the use of superconducting ILC-type cavities to accelerate *both* protons and electrons, which considerably increases its physics potential. Polarized electrons and positrons can be used to study the structure of composite particles and the dynamics of strong interactions, as well as to search for new physics beyond the Standard Model.

2 The Proposed Proton/Electron Facility at KEK

The main 'bottleneck' limiting the beam power in circular machines is caused by space charge effects that produce beam instabilities. Such a 'bottleneck' exists at the J-PARC proton synchrotron complex, and is also intrinsic to the 'proton drivers' envisaged at CERN and Fermilab. To increase maximally the beam power of a 'proton driver', it is proposed to build a facility consisting solely of a low-energy injector linac and a high-energy *pulsed* superconducting linac. Pulsed operation is preferred over the CW mode (continuous wave, 100% duty) mainly because the former allows the use of rf cavities with high accelerating gradients. This would considerably reduce the overall length of the machine, which is limited by the size of the KEK site.

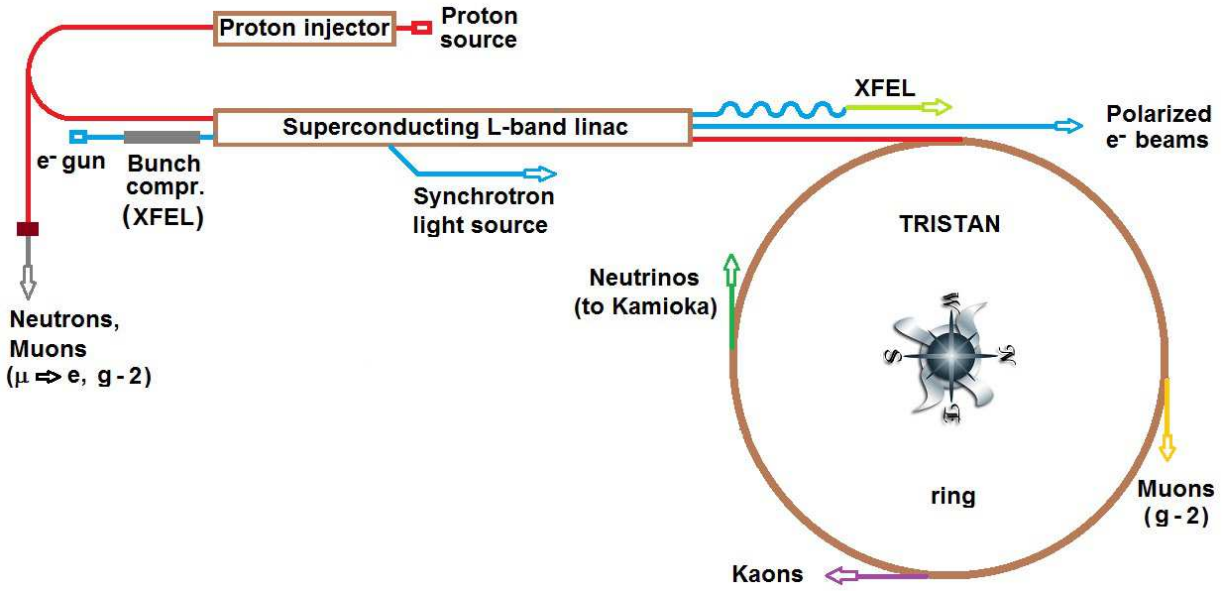

Figure 1: The layout of the proposed multi-purpose proton/electron facility at KEK. The Tristan ring would initially be equipped only with magnets capable of steering the proton bunches, accelerated by the superconducting linac, to various fixed targets.

The layout of the proposed proton/electron facility at KEK is shown in Fig. 1. A 2.5 GeV proton linac (PI) serves both as an injector to a superconducting linac (SCL) and a source of proton beams that can be used to copiously produce neutrons and muons. Protons accelerated by the SCL to 20 GeV are transferred through the KEK Tristan ring in order to create beams for various fixed-target experiments. At a later stage, a 70 GeV proton synchrotron could be installed inside the Tristan ring. The SCL, comprising 1.3 GHz superconducting ILC-type rf cavities, can also accelerate polarized or unpolarized electron bunches. After acceleration, electrons may traverse an XFEL undulator, or could be used to produce polarized positrons. An SCL-based XFEL and a synchrotron light source for applications in materials science and medicine are also envisaged.

The proposed facility would be constructed using the existing KEK accelerator infrastructure. As shown in Fig. 2, the present KEK linac tunnel and klystron gallery could be extended to increase the length, and hence the maximum energy, of each linac in Fig. 1. The cryomodules, RF sources and cryogenic plant units of the proposed linac complex would be installed inside these extended structures (see Fig. 3). The Tristan ring (TR) would initially be equipped only with magnets capable of steering the SCL proton bunches to various fixed targets. The four 200 m-long straight sections of the TR, each with an experimental hall in the middle (see Fig. 2), would house beam lines and detectors.

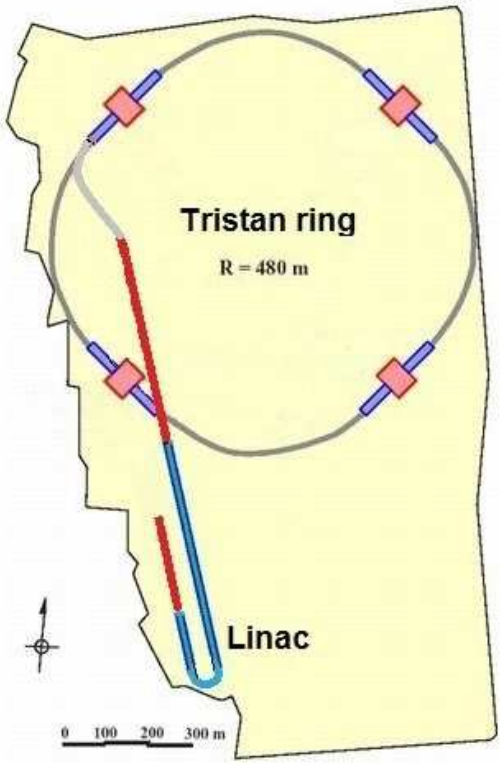

Figure 2: A sketch of the KEK site showing the Tristan ring and the existing electron linac (in blue). The lines drawn in red indicate possible extensions of the present linac tunnels. Alternatively, a new underground linac tunnel could be excavated at a greater depth if demanded by radiation safety requirements.

The beam power of a pulsed linear accelerator is given by the expression

$$\mathcal{P}_{\rm beam}\,[\rm MW] = \rm E_b\,[MV] \times \mathit{I}\,[A] \times \tau_p\,[s] \times \mathcal{R}\,[Hz] \tag{1}$$

where $\mathcal{P}_{\rm beam}$ is the *beam power*, $\rm E_b$ is the *beam energy*, I is the *average current per pulse*, τ_p is the *beam pulse length*, and $\mathcal{R}$ is the *repetition rate*. The *duty cycle* of a pulsed linac is $\mathcal{D} \equiv \tau_p \mathcal{R}$. Using the values from Table 1, and assuming $\rm E_b = 20$ GeV, one obtains $\mathcal{D} = 0.024$ and

$$\mathcal{P}_{\rm beam} = 20,000\,\rm MV \times 31\,mA \times 1.2\,ms \times 20\,s^{-1} \approx 15\,MW \tag{2}$$

The beam parameters in Table 1 are mutually constrained by the following relations: The number of protons per second $N = \mathcal{P}/\rm E_b$ and the number of protons per pulse $N_p = N/\mathcal{R}$; the average current per pulse is $I \equiv (N_p \times 1.6 \times 10^{-19}\,\rm C)/\tau_p$. The klystron pulse length is the sum of the rf cavity fill time (current dependent) and the beam pulse length: $\tau = \tau_f + \tau_p$. For ILC-type cavities and $I \sim 30$ mA, $\tau_f \approx 0.3$ ms. Since $\tau = 1.5$ ms, the beam pulse length $\tau_p \approx 1.2$ ms.

2.1 Main Characteristics of an ILC-Type Linac

The main characteristics of a linear accelerator are determined by the properties of its rf source (klystrons) and accelerating cavities. For a pulsed ILC-type superconducting linac, one of the currently available rf sources is the *Toshiba* E3736 *Multi-Beam Klystron* [4]. This source has the following well-tested specifications: *rf frequency* – 1.3 GHz; *peak rf power* – 10 MW; *average power* – 150 kW; *efficiency* – 65%; *pulse length* – 1.5 ms; *repetition rate* – 10 Hz. If the repetition rate of the Toshiba klystron is increased by a factor of two, while its peak power is reduced by the same

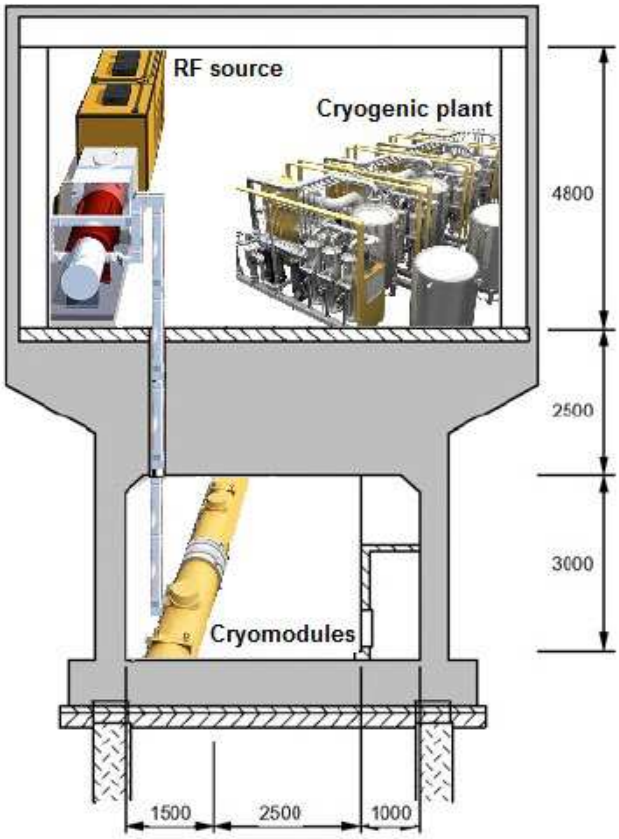

Figure 3: Front view of the linac tunnel and the klystron gallery housing the cryomodules, RF sources and cryogenic plant units of the proposed superconducting linac complex.

factor (thus keeping the average power constant) one obtains the klystron specifications presented in Table 1. For such a klystron, a suitable 20 Hz *pulse modulator* has to be developed.

A very important parameter that determines, to a large extent, the power conversion efficiency of a klystron is its *perveance*, defined by

$$K \equiv \frac{I_0}{U^{3/2}} \tag{3}$$

In this expression, I_0 is the beam current and U is the anode voltage. Since there is an upper limit to the applied voltage, low perveance can be only obtained by operating with low currents. For single-beam klystrons, this requirement is not compatible with the need for high ouput power. With this in mind, *multi-beam klystrons* (MBK) were originally developed in the 1960s [5]. An MBK is a parallel assembly of low-current (low-perveance) *beamlets* within a common rf structure, which efficiently generates high output power. Using Eq. (3), the output rf power of an MBK can be expressed as

$$\mathcal{P}_{\rm k} = \eta I_0 U = \eta K U^{5/2} \tag{4}$$

where η is the klystron *efficiency* and $I_0 = N_{\rm b} I_{\rm b}$ is the total beam current; $N_{\rm b}$ is the number of beamlets and $I_{\rm b}$ is the current carried by each beamlet. For Toshiba's E3736 MBK, $\eta = 65\%$, $U = 116$ kV and $I_0 = 134$ A. Hence, $K = 3.4 \times 10^{-6}$ A/V$^{3/2}$, klystron's peak power $\mathcal{P}_{\rm k} = 10$ MW and its average power $\overline{\mathcal{P}}_{\rm k} \equiv \mathcal{P}_{\rm k} \times \mathcal{D} = 150$ kW. Since the klystron has six beamlets, $I_{\rm b} = 22.3$ A.

The basic properties of a 1.3GHz superconducting ILC-type cavity are presented, e.g., in [6]. There are two important parameters that characterize rf cavities: the *accelerating gradient* $\rm E_{acc}$ and the *unloaded quality factor* Q_0. The former is a measure of how much the energy of a particle is increased over a given length of the linac (typically expressed in units of MV/m), while the latter specifies how well the cavity can sustain the stored rf power. A higher value of Q_0 implies a

Table 1: Parameters of the SC linac

Beam energy	20 GeV
Beam power	15 MW
Repetition rate	20 Hz
Protons per pulse	2.3×10^{14}
Beam pulse length	1.2 ms
Average current per pulse	31 mA
Duty cycle	2.4 %
RF frequency	1.3 GHz
Klystron average power	150 kW
Klystron peak power	5 MW
Klystron pulse length	1.5 ms
Effective accelerating gradient	20 MV/m
Peak power per coupler	460 kW

lower rate of power loss realtive to the stored energy.[1] ILC-type cavities must have a nominal Q_0 greater than 1×10^{10} (a dimensionless parameter) at $\mathrm{E_{acc}} = 31.5$ MV/m.

Each ILC-type cryomodule for the proposed SCL would contain eight niobium 9-cell cavities and a quadrupole magnet at its centre. Other major components of such a cryomodule are the vacuum vessel, thermal and magnetic shields, cryogenic piping, interconnections, etc. The inactive spaces between cavities or cryomodules (the 'packing fraction') are responsible for a substantial reduction in the average accelerating gradient of the linac.

The average *usable* accelerating gradient in ILC-type cavities is $\overline{\mathrm{E}}_{\mathrm{acc}} = 29.3 \pm 5.1$ MV/m (see Fig. 4). Taking into account an estimated linac 'packing fraction' of about 70%, the effective accelerating gradient of the SCL is $\mathrm{E_{eff}} \approx 20$ MV/m. This implies that the total length of a 20 GeV linac is ~ 1000 m.

Since the length of an ILC 9-cell cavity is 1m, a linac with $\mathrm{E_b} = 20$ GeV would require $N_{\mathrm{cav}} = (20,000 \text{ MeV})/(29 \text{ MeV}) \approx 690$ cavities. Hence, the average input rf power per cavity $\overline{\mathcal{P}}_{\mathrm{cav}} = \mathcal{P}_{\mathrm{beam}}/N_{\mathrm{cav}} \approx 22$ kW, and the corresponding peak power $\mathcal{P}_{\mathrm{cav}} \equiv \overline{\mathcal{P}}_{\mathrm{cav}}/\mathcal{D} = 916$ kW. Although this value is acceptable for a pulsed linac with $\mathcal{D} \sim 2\%$, it would be prudent to use two rf couplers per cavity. In that case the peak rf power per coupler would be about 460 kW.

For $\mathrm{E_{acc}} = 30$ MV/m, ohmic losses in an ILC 9-cell cavity amount to $\mathcal{P}_{\mathrm{c}} = 100$ W in the CW mode of operation, but only $\mathcal{P}_{\mathrm{c}} = (100 \times \mathcal{D})\,\mathrm{W} = 2.4\,\mathrm{W}$ (plus static loss) in the pulsed mode with a duty factor $\mathcal{D} = 0.024$. Because of large ohmic losses, which scale with the square of the accelerating gradient, $\mathrm{E_{acc}}$ is limited to about 15 MV/m for linacs operated in the CW mode. As already mentioned, pulsed operation of the SCL is preferred over the CW mode mainly because the former allows the use of rf cavities with high accelerating gradients. This would considerably reduce the overall length of the linac, which is limited by the size of the KEK site.

[1] The Q factor of an rf cavity is defined as $Q \equiv 2\pi \times$(energy stored/energy dissipated per cycle). For large values of Q, the Q factor is approximately the number of oscillations required for the energy of a freely oscillating system to fall off to $\mathrm{e}^{-2\pi}$, or 0.2%, of its original value.

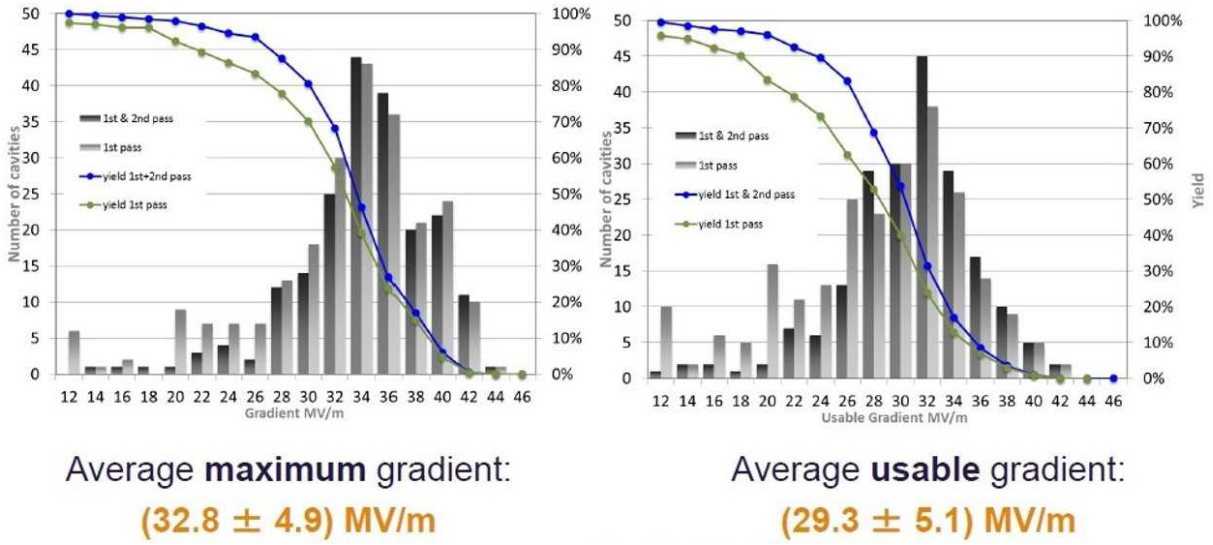

Figure 4: Measured accelerating gradients of 207 superconducting ILC cavities; credit: D. Reschke.

2.2 Proton Injector (PI)

A typical ~ 1 GeV proton linear accelerator (see Fig. 5) consists of three main sections:

- *Front end*, comprising a proton source and a radiofrequency quadrupole accelerator;
- *Medium-velocity linac*, which accelerates proton beams to ~ 100 MeV;
- *High-velocity linac*, which accelerates protons to energies exceeding 1 GeV.

The most complex part of a proton linac is the low-energy (low-β) section, situated between the proton (or ion) source and the first drift-tube-based accelerating section. The continuous beam of protons coming from an *electron cyclotron resonance* (ECR) source [7] has to be focused, bunched and accelerated in the first rf structure. These three essential functions are nowadays successfully performed by *radio frequency quadrupoles* (RFQ) [8]. However, the beam has to be shrunk before it can be fed into an RFQ. This is accomplished within a low-energy beam transport (LEBT) section by means of cylindrical magnets (solenoids).

As soon as the beam is bunched — which is essential for further acceleration — it enters a medium-energy beam transport (MEBT) section, where it is collimated and steered from the RFQ into the medium-velocity linac (MVL). The MEBT may also contain a number of buncher cavities. Inside the MVL, the beam is accelerated to about 100 MeV ($\beta \sim 0.1$ to 0.5). The MVL usually contains normal-conducting *drift-tube linac* (DTL) and *cell-coupled drift tube linac* (CCDTL) structures. A DTL incorporates accelerating components of increasing length in order to match precisely the increase in beam velocity, while quadrupole magnets provide strong focusing. The main advantage of using CCDTL structures is that they provide longitudinal field stability.

High-velocity linac (HVL) structures accelerate the beam to energies around 1 GeV. They consist either of normal-conducting *side-coupled linac* (SCL) structures[2] or superconducting *elliptical cavities*. The latter offer some advantages over the former, such as higher accelerating gradients and lower operating costs. The superconducting HVL can also feature *spoke resonators*, characterized by their simplicity, high mechanical stability and compact size [9].

One of the main concerns in the design of a high-power proton linac is to restrict beam losses. A careful beam dynamics study is therefore needed in order to avoid halo formation, a major source of beam loss. Another important issue is the preservation of beam emittance [11].

[2]The main reason for using these $\pi/2$-mode structures is that long chains of coupled cavities are often required for an efficient use of high-power rf sources [9].

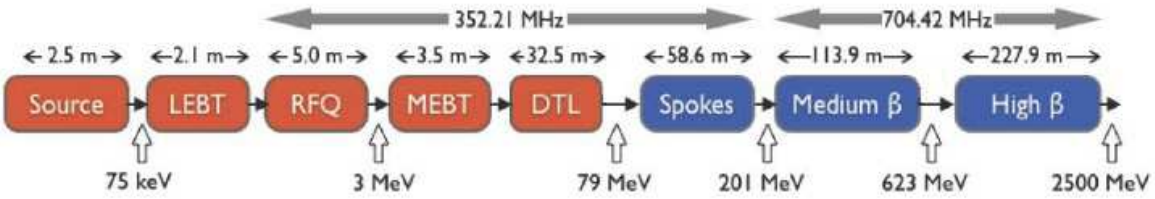

Figure 5: As an example of a typical ~ 1 GeV proton linear accelerator, a block diagram of the ESS linac design is shown [10]. The RFQ and DTL structures are normal-conducting, while the spoke resonator and elliptical cavities are superconducting. The transverse beam size along the linac varies in the range 1–4 mm, and the bunch length decreases from 1.2 cm to 3 mm towards the end of the linac.

High-power proton linear accelerators have a wide range of applications including spallation neutron sources, nuclear waste transmutation, production of radioisotopes for medical use, etc. A number of laboratories worldwide have expressed interest in building 'proton drivers' that would primarily deliver high-intensity neutrino, kaon and muon beams [12, 13]. The physics potential of such a facility is discussed in the next section.

3 Physics at the Proposed Facility

The physics potential of a multi-MW 'proton driver' is extensively discussed, for instance, in [14]. This note is mainly concerned with the application of a high-intensity proton source to investigate the properties of long-baseline neutrino oscillations. A unique feature of the proposed facility is the use of a superconducting linac to accelerate *both* protons and electrons, which considerably increases its physics potential. As described in [15, 16], polarized electron and positron beams can be used to study the structure of composite particles and the dynamics of strong interactions, as well as to search for new physics beyond the Standard Model.

3.1 Neutrino Flavor Oscillations and Leptonic CP Violation

The universe contains about a billion neutrinos for every quark or electron. The three known neutrino species ('flavors') are named after their partner leptons in the Standard Model: *electron neutrino*, *muon neutrino* and *tau neutrino*. The observed transformation of one neutrino flavor into another ('*neutrino oscillation*') indicates that these ubiquitous particles have finite masses [3]. Cosmological data suggest that the combined mass of all three neutrino species is a million times smaller than that of the next-lightest particle, the electron [17].

The phenomenon of neutrino oscillations implies not only the existence of neutrino mass, but also of *neutrino mixing*. That is, the neutrinos of definite flavor are not particles of definite mass (mass eigenstates), but coherent quantum-mechanical superpositions of such states. Converesely, each neutrino of definite mass is a superposition of neutrinos of definite flavor. Neutrino mixing is large, in striking contrast to quark mixing. *Whatever the origin of the observed neutrino masses and mixings, it implies a profound modification of the Standard Model.*

Mathematically, the phenomenon of neutrino mixing can be expressed as a unitary transformation relating the flavor and mass eigenstates. The neutrino oscillation rate depends, in part, on (1) the difference between neutrino masses and (2) the three parameters in the transformation matrix known as *mixing angles*. The complex phase factors in the transformation matrix (also called *mixing matrix*) are associated with the violation of CP symmetry in the lepton sector. The size of the CP violation is determined both by the phases and the mixing angles.

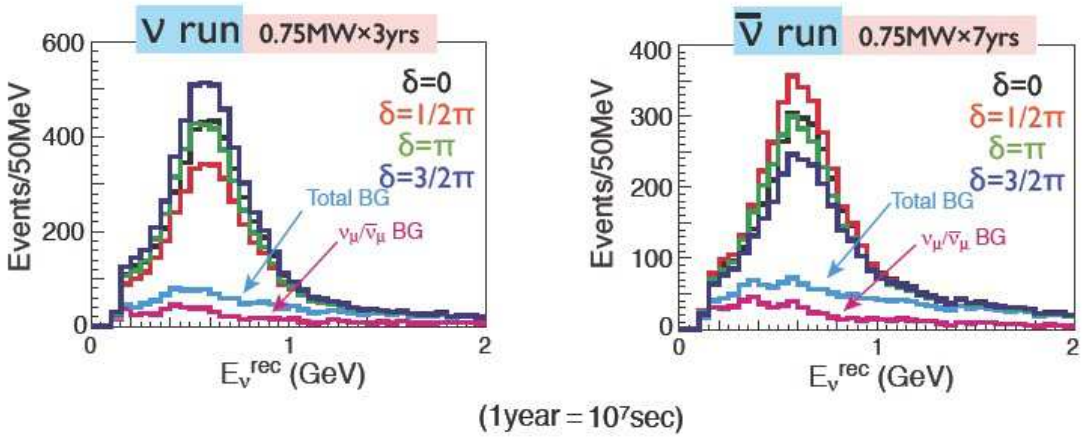

	Signal ($\nu_\mu \to \nu_e$ CC)	Wrong sign appearance	$\nu_\mu/\bar{\nu}_\mu$ CC	$\nu_e/\bar{\nu}_e$ contamination	NC
ν ($2.25\text{MW} \cdot 10^7\text{s}$)	3,560	46	35	880	649
$\bar{\nu}$ ($5.25\text{MW} \cdot 10^7\text{s}$)	1,959	380	23	878	678

Figure 6: Predicted yield of ν_e and $\bar{\nu}_e$ 'appearance events' inside the 0.5 Mt fiducial volume of the proposed Hyper-Kamiokande (HK) detector, assuming that the beam power of the 30 GeV proton synchrotron at J-PARC is increased to 0.75 MW (δ is a CP-violating parameter); credit: the T2K Collaboration. Over the same data taking period, beams produced at the proposed 15 MW 'proton driver' would yield roughly the same number of 'appearance events' inside the 0.022 Mt fiducial volume of the existing Super-Kamiokande detector (the same baseline as for HK).

Experiments with high-intensity neutrino beams are designed primarily to explore the mass spectrum of the neutrinos and their properties under the CP symmetry, and thus provide a deeper insight into the nature of these elusive particles and their role in the universe. For instance, if there is experimental evidence for CP violation in neutrino oscillations, it could be used to explain the observed asymmetry between matter and antimatter [18].

The proposed T2HK (Tokai-to-Hyper-Kamiokande) project is a natural extension of the T2K (Tokai-to-Super-Kamiokande) neutrino oscillation experiment [19]. Hyper-Kamiokande (HK), a water Cherenkov detector with a fiducial mass of about 0.5 million metric tons (0.5 Mt), would serve as a far detector for neutrino beams produced at the J-PARC accelerator complex, situated at a distance $L_1 \approx 300$ km from Kamioka. Since the baseline L_1 is relatively short, the matter-induced neutrino mixing is rather small, which implies a weak sensitivity to the neutrino mass hierarchy. The T2HK Collaboration intends to resolve this hierarchy by virtue of matter-enhanced oscillations of atmospheric neutrinos traversing the Earth [19, 20].

Under the assumption that the beam power of the 30 GeV proton synchrotron at J-PARC can be increased to 0.75 MW, the T2HK experiment would deliver about 5500 ν_e and $\bar{\nu}_e$ 'appearance events' in the HK detector within ten years of data taking (see Fig. 6). *The same event yield would be obtained within a year using the* HK *detector and the proposed* KEK '*proton driver*'.

Alternatively, a 100 kiloton water Cherenkov detector could be built at Okinoshima, located along the T2K beamline at a distance $L_2 \approx 650$ km from KEK. Using the proposed 'proton driver', the detector at Okinoshima as well as Super-Kamiokande, the neutrino mass hierarchy could be determined either by comparing the ν_e appearance probabilities measured at the two vastly different baseline lengths L_1 and L_2, or by measuring at L_1 and L_2 the neutrino energy of the first oscillation maximum. Once the mass hierarchy is determined, the CP-violating phase in the mixing matrix can be measured with a precision of $\pm 20°$, assuming that 2.5×10^{21} protons are delivered on target for both ν_e and $\bar{\nu}_e$ beams [21].

The main challenge in the design of a multi-MW neutrino beam facility is to build a *proton target* that could dissipate large amounts of deposited energy, withstand the strong pressure waves created by short beam pulses, and survive long-term effects of radiation damage. Simulation studies of the pion production and energy deposition in different targets (liquid mercury jet, tungsten powder jet, solid tungsten bars and gallium liquid jet) are presented in [22]. Those studies also provided estimates of the amount of concrete shielding needed to protect the environment from the high radiation generated by each target. A proof-of-principle demonstration of a 4 MW target station comprising a liquid mercury jet inside a 20 T solenoidal magnetic field is described in [23]. A 15 MW proton beam could be separated by a series of magnets into four beam lines. Each of the four beams would be focused by a series of quadrupoles and correctors to an assembly consisting of four targets and the same number of magnetic horns (see, e.g., [24]).

To maximize the discovery potential of a neutrino beam facility, it is important to properly design the *magnetic horn* that focuses the charged particles produced in the proton target. For proton beam pulses lasting 1 ms, a DC horn has been designed by Yukihide Kamiya of KEK [25]. The toroidal magnetic field of the horn, characterized by $\mathrm{B}(r) = \text{const.}$, is generated by hollow aluminium conductors containing water. The strength of the magnetic field $\mathrm{B} = 0.2$ T, and its length $\ell = 5$ m; hence, $\mathrm{B} \cdot \ell = 1\ \mathrm{T} \cdot \mathrm{m}$. The radius of the magnet, r, is determined by $r = L\tan(\theta) + \ell\tan(\theta/2)$, where $\theta \approx 0.03 + 0.3/p$ is the initial angle a charged pion makes with respect to the proton beam direction, L is the distance from the target to the horn, and p is the pion momentum. For example, if $L = 5$ m then $r \approx 5$ m. The total power generated in the conductors is about 10 MW.

3.2 Physics with Polarized Electrons and Positrons

Electron and positron beams, polarized and/or unpolarized, can be used to study the structure of composite particles and the dynamics of strong interactions, as well as to search for new physics beyond the Standard Model. A detailed description of the physics potential of a facility that can provide such beams (e.g., the upgraded CEBAF facility at Jefferson Lab or the proposed KEK superconducting linac) is presented in [15, 16].

Polarized positrons are created in a conversion target by circularly polarized photons, which themselves are produced when polarized laser light is Compton-backscattered on a high-energy electron beam [26]. Circularly polarized photons can also be produced by bremsstrahlung from polarized electrons [27]. Using polarized electrons and positrons, the *nucleon electromagnetic form factors* and *generalized parton distributions* can be determined in a model-independent way [16].

Among the physics topics discussed in [15], parity violation in electron-electron (Møller) scattering is of particular interest. Møller scattering is a purely leptonic process that allows high-precision tests of the Standard Model. At four-momentum transfers much smaller than the mass of the Z boson ($q^2 \ll \mathrm{M_Z^2}$), the parity-violating asymmetry, $\mathcal{A}$, is dominated by the interference between the electromagnetic and neutral weak amplitudes [28]. By definition,

$$\mathcal{A} \equiv \frac{\mathrm{d}\sigma_\mathrm{R} - \mathrm{d}\sigma_\mathrm{L}}{\mathrm{d}\sigma_\mathrm{R} + \mathrm{d}\sigma_\mathrm{L}} \approx \frac{f_\mathrm{Z}^\mathrm{R} - f_\mathrm{Z}^\mathrm{L}}{f_\gamma} \tag{5}$$

In this expression, $\mathrm{d}\sigma_\mathrm{R}$ ($\mathrm{d}\sigma_\mathrm{L}$) is the differential cross-section for right-handed (left-handed) electron scattering on an unpolarized target:

$$\mathrm{d}\sigma_\mathrm{R,L} \propto |f_\gamma + f_\mathrm{Z}^\mathrm{R,L}|^2 \approx |f_\gamma|^2 + 2 f_\gamma f_\mathrm{Z}^\mathrm{R,L} \tag{6}$$

where f_γ and $f_\mathrm{Z}^\mathrm{R,L}$ are the scattering amplitudes with γ and Z exchange, respectively. From the four Feynman diagrams in Fig. 6 of [29], one can readily obtain the Born amplitudes for Møller scattering mediated by photons and Z bosons. The weak neutral current amplitudes are functions of the weak mixing (or Wienberg) angle θ_w, which relates the weak coupling constants g_w and

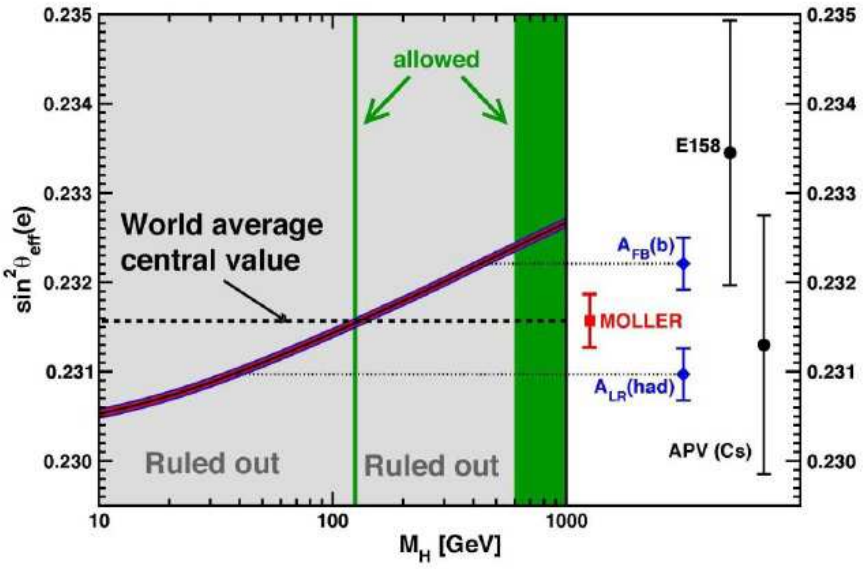

Figure 7: Indirect constraints on the Higgs-boson mass, $\mathrm{M_H}$, from the most precise high q^2 (blue) and low q^2 (black) measurements of $\sin^2\theta_\mathrm{w}$, evolved to the same energy scale ($q^2 = \mathrm{M_Z^2}$); credit: Jens Erler and [15]. *Green bands*: allowed $\mathrm{M_H}$ regions; *Red curve*: theory predictions for $\sin^2\theta_\mathrm{w}$ vs $\mathrm{M_H}$; *Dashed line*: average value of $\sin^2\theta_\mathrm{w}$ from all electroweak asymmetry data; *Red*: expected measurement precision (placed at an arbitrary y-axis value) of the MOLLER experiment [31], in which a 11 GeV longitudinally polarized electron beam would scatter on atomic electrons in a liquid hydrogen target.

g_Z to the electromagnetic coupling constant. As shown in [29], the polarization asymmetry for polarized electron scattering on an unpolarized target is given by

$$\mathcal{A}^{\mathrm{Born}} = m_e \mathrm{E} \frac{G_\mathrm{F} Q_\mathrm{w}^e}{\sqrt{2}\pi\alpha} \mathcal{F}(\theta) \tag{7}$$

where m_e is the mass of the electron, E is the incident beam energy, G_F is the Fermi coupling constant characterizing the strength of the weak interaction, α is the fine structure constant, and $\mathcal{F}(\theta)$ is a function of the scattering angle in the center-of-mass frame. The *weak charge* of the electron, $Q_\mathrm{w}^e = 1 - 4\sin^2\theta_\mathrm{w}$, is proportional to the product of the electron's vector and axial-vector couplings to the Z boson.

Since the value of $\sin^2\theta_\mathrm{w}$ is close to 1/4, there is an enhanced sensitivity of $\mathcal{A}$ to small changes in the Weinberg angle. The value of θ_w varies as a function of the four-momentum transfer, q, at which it is measured. This variation, or 'running', is a key prediction of the Standard Model. The one-loop *electroweak radiative corrections* to $\mathcal{A}^{\mathrm{Born}}$ (calculated once the renormalized parameters in (7) are properly defined) reduce its Born value by ∼40%. This effect can be attributed to an increase of $\sin^2\theta_\mathrm{w}(q^2)$ by 3% as the four-momentum transfer 'runs' from $q^2 = \mathrm{M_Z^2}$ to $q^2 \approx 0$ [30].

Many of the electroweak meaurements obtained over the past three decades may be combined to provide a global test of consistency with the SM. Since the Higgs-boson mass affects the values of electroweak observables through radiative corrections, it is of fundamental importance to test the agreement between the directly measured value of $\mathrm{M_H}$ and that inferred from the measurements of electroweak parameters $\sin^2\theta_\mathrm{w}$ (see Fig. 7), $\mathrm{M_W}$ and $\mathrm{M_{top}}$. High-precision electroweak measurements, therefore, represent a natural complement to direct studies of the Higgs sector.

Apart from providing a comprehensive test of the SM, precision measurements of weak neutral current interactions at $q^2 \ll \mathrm{M_Z^2}$ also allow indirect access to new physics phenomena beyond the TeV energy scale. For instance, such measurements can be used to look for hypothetical Z' bosons, 4-fermion contact interactions, or very weekly coupled low-mass 'dark bosons' [32].

3.3 Rare Kaon Decays

Some of the most important discoveries in particle physics emerged from studies of K mesons ('kaons'), in particular *neutral kaons*. The neutral K meson, K^0, and its antiparticle, $\bar{K}^0$, form a remarkable quantum-mechanical two-state system that has played a significant role in the development of the Standard Model [33].

In 1953, it was shown that the observed 2π and 3π decay modes of the charged kaon required the parent particles to have opposite intrinsic parities. This suggested that parity may not be conserved. Three years later, experiments demonstrated that parity was indeed violated in weak interactions. The first indication that parity violation was accompanied by a failure of charge conjugation was seen in 1964, when one 2π event was detected for every 500 or so common 3π decays of the long-lived neutral kaon, $K^0_{\rm L}$. The concept of *strangeness*, introduced in 1953 to explain the anomalously long lifetimes of K mesons, was crucial for the development of the quark model of particles. In 1970, the smallness of the observed branching ratio for $K^0_{\rm L} \to \mu^+\mu^-$, implying the absence of strangeness-changing neutral currents, led to the prediction of a fourth quark, the *charm* quark. The sensitivity of K^0-$\bar{K}^0$ mixing to energies higher than the kaon mass scale was used soon thereafter to predict the mass of the charm quark (discovered in 1974).

CP violation was introduced in the SM by increasing the number of quark and lepton families to at least three (M. Kobayashi and T. Maskawa, 1973). This idea became very attractive with the subsequent discovery (in 1977) of the *bottom* quark, which forms, together with the *top* quark (discovered in 1995), a third family of quarks. It is a remarkable property of the Kobayashi-Maskawa model that *quark mixing* and CP violation are intimately related.

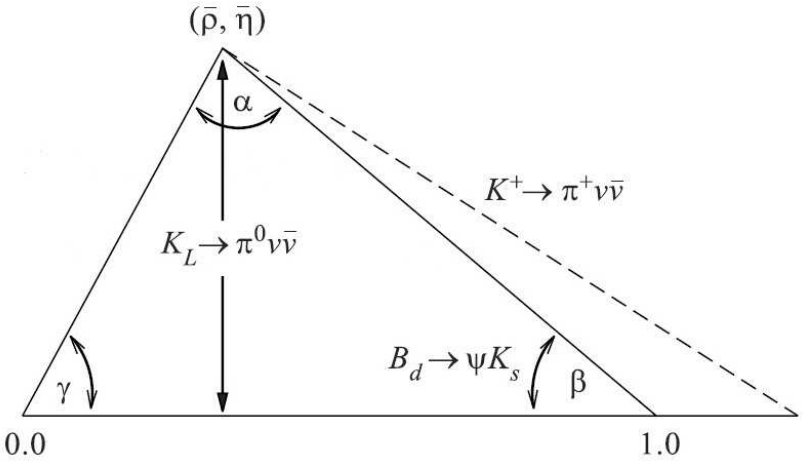

Figure 8: Unitarity triangle from $K \to \pi\nu\bar{\nu}$ decays. The displacement of the bottom-right vertex is due to the charm-quark contribution to $K^+ \to \pi^+\nu\bar{\nu}$.

A deeper insight into CP violation is expected to be gained from precision measurements of rare kaon decays such as $K^0_{\rm L} \to \pi^0\nu\bar{\nu}$ and $K^+ \to \pi^+\nu\bar{\nu}$. Both decays are theoretically 'clean' because hadronic transition amplitudes are matrix elements of quark currents between mesonic states, which can be extracted from the leading semileptonic decays using isospin symmetry. Since photons do not couple to neutrinos, $K \to \pi\nu\bar{\nu}$ decays are entirely due to second-order weak processes determined by Z-penguin and W-box diagrams [33].

The process $K^0_{\rm L} \to \pi^0\nu\bar{\nu}$ proceeds almost entirely through direct CP violation, and is completely determined by 'short-distance' one-loop diagrams with top quark exchange. The Standard Model predicts its branching ratio to be $\mathcal{B}(K^0_{\rm L} \to \pi^0\nu\bar{\nu}) = (2.43 \pm 0.39) \times 10^{-11}$ [34]. This decay is an important source of information on higher-order effects in electroweak interactions, and therefore can serve as a probe of physics beyond the Standard Model (see [35] and references therein).

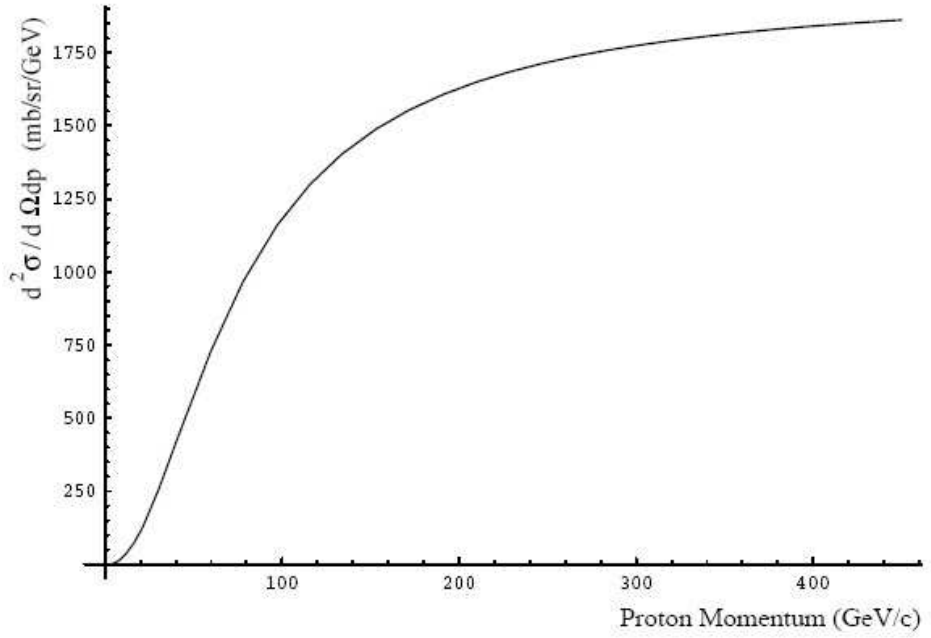

Figure 9: Differential cross-section for the production of $K_{\rm L}^0$ as a function of the incident proton momentum [35]. The cross-section is for a beryllium target in the forward direction, and with kaon momenta integrated from 2 to 20 GeV. The estimate is based on the empirical Sanford-Wang formula, using $\mathrm{d}\sigma(K_{\rm L}^0) = [\mathrm{d}\sigma(K^+) + 3\mathrm{d}\sigma(K^-)]/4$.

The decay $K^+ \to \pi^+\nu\bar{\nu}$ receives both CP-conserving and CP-violating contributions. It has theoretical uncertainties that are somewhat larger than those in the process $K_{\rm L}^0 \to \pi^0\nu\bar{\nu}$. Since both decays involve one-loop Feynman diagrams with top quark exchange, they can yield valuable measurements of the CKM matrix elements $|V_{td}|$ and $|V_{ts}|$. The quantity $\mathrm{Im}V_{ts}^*V_{td}$, which can be obtained from $K_{\rm L}^0 \to \pi^0\nu\bar{\nu}$ alone, plays a central role in the phenomenology of CP violation in K decays; this quantity is related to the *Jarlskog parameter*, the invariant measure of CP violation in the Standard model [33, 36].

By measuring the branching ratios of both $K \to \pi\nu\bar{\nu}$ decay modes, the *unitarity triangle* of the CKM matrix can be completely determined (see Fig. 8), provided the matrix element V_{cb} and the top quark mass are known [36]. Of particular interest is the unitarity triangle parameter $\sin 2\beta$, which can also be determined from the decay $B_d \to \Psi \mathrm{K}_s$. Both determinations of this parameter have to coincide if the Standard Model is valid [35].

The decay $K_{\rm L}^0 \to \pi^0\nu\bar{\nu}$ has not yet been observed. The KOTO experiment at J-PARC [37], the aim of which is to study this decay mode, had its first physics run in May 2013. The current branching ratio measurement of the charged decay mode, $\mathcal{B}(K^+ \to \pi^+\nu\bar{\nu}) = (17.3^{+11.5}_{-10.5}) \times 10^{-11}$, is based on the seven candidate events observed by the experiment E787/E949 at Brookhaven [38]. This result is consistent with $(7.8 \pm 0.80) \times 10^{-11}$, the value predicted by the SM [34]. The proposed ORKA experiment at Fermilab will use the stopped-kaon technique of its predecessor E787/E949 to detect about 1000 $K^+ \to \pi^+\nu\bar{\nu}$ decays, and measure the corresponding branching ratio with a precision of 5% [39]. The NA62 experiment at CERN will rely on a complementary decay-in-flight technique to detect about 100 $K^+ \to \pi^+\nu\bar{\nu}$ decays [40].

As shown in Fig. 9, the kaon yield rises rapidly as a function of the incident proton momentum. From the figure one infers that the minimum energy of the proton beam should be about 20 GeV, for otherwise the kaon yield would be severely reduced. At the proposed KEK facility, a 70 GeV proton synchrotron could be installed, at a later stage, inside the Tristan ring in order to increase the proton beam energy — albeit at the cost of a considerably lower beam power. For a given kaon yield, the required beam power would be lowest at energies between 30 and 100 GeV [35].

3.4 A Novel g-2 Experiment with Ultra-Slow Muons

A charged elementary fermion has a *magnetic dipole moment* $\boldsymbol{\mu} = g_s(q/2m)\boldsymbol{s}$ aligned with its spin $\boldsymbol{s}$. The proportionality constant g_s is the Landé g-factor, q is the charge of the particle and m is its mass. Dirac's theory of the electron predicts that $g_s = 2$. For the *electron* (e), *muon* (μ) and *tau lepton* (τ), this prediction differs from the observed value by a small fraction of a percent. The difference is the *anomalous magnetic moment*; the anomaly is defined by $a \equiv (g_s - 2)/2 \sim 10^{-3}$. In the Standard Model, three distinct classes of Feynman diagrams contribute to the value of the anomaly for each lepton species: (1) the dominant QED terms that contain only leptons and photons; (2) terms that involve hadrons; and (3) electroweak terms containing the Higgs, W and Z bosons. The muon anomaly a_μ is about $(m_\mu/m_e)^2 \sim 43\,000$ times more sensitive to the existence of yet unknown heavy particles than the electron anomaly a_e. The value of a_μ (a_e) is sensitive to new physics at the scale of a few hundred GeV (MeV) [41].

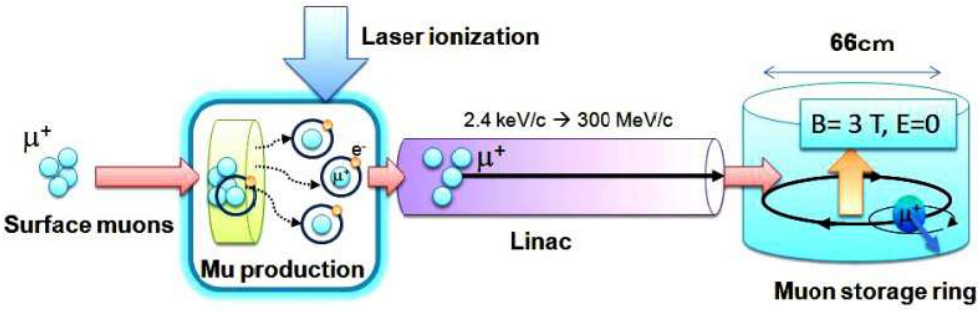

Figure 10: The conceptual design of a proposed experiment to measure the *magnetic dipole moment* $\boldsymbol{\mu}_\mu = g_s(q/2m)\boldsymbol{s}$ and the *electric dipole moment* $\boldsymbol{d}_\mu = \eta(q\hbar/2m)\boldsymbol{s}$ of the muon [42].

The current experimental uncertainty on a_μ is ± 0.54 ppm. In a novel g-2 experiment, the aim of which is to reduce this uncertainty to ± 0.1 ppm (see Fig. 10), 3 GeV protons impinge on a graphite target and produce pions that are stopped in the target. Some of the positive pions are brought to rest near the surface of the target, where they decay into positive muons with momenta $p_\mu = 30\,\mathrm{MeV/c}$ and 100% spin polarization. The muons are collected using a large-aperture solenoid and transported to a silica-aerogel target in which they form muonium (electron–μ^+) atoms. As the atoms slowly diffuse from the target, they are ionized by a pulsed laser to produce 50% polarized muons with very low momenta.[3] Those 'ultra-slow' muons (4×10^4/pulse) are then accelerated to $p_\mu = 300\,\mathrm{MeV/c}$ by two linacs, and injected into a magnetic storage ring that contains a 3 T solenoid with a diameter of 66 cm. After injection, the muons circulate orthogonal to the magnetic field $\mathbf{B}$. An orbiting muon decays within 6.6 μs into a positron, a neutrino and an antineutrino: $\mu^+ \to \mathrm{e}^+ + \nu_e + \bar{\nu}_\mu$.

The highest-energy positrons, preferentially emitted parallel to the muon spin direction in the μ^+ rest frame, are Lorentz-boosted to become the highest-energy positrons in the lab frame. Hence, the angular distribution of those positrons has its maximum in the direction of the muon spin [17]. By measuring the energy and time distributions of positrons one can determine the average spin direction. The time spectrum will show the muon lifetime modulated by the spin precession frequency. The relative precession of the spin with respect to the direction of the particle velocity $\boldsymbol{u}$ is given by $\boldsymbol{\omega}_a + \boldsymbol{\omega}_\eta \propto a_\mu \mathbf{B} - (\eta/2)(\boldsymbol{\beta}\times\mathbf{B})$, where $\boldsymbol{\omega}_a$ and $\boldsymbol{\omega}_\eta$ arise from a_μ and $\boldsymbol{d}_\mu$, respectively, and $\boldsymbol{\beta} \equiv \boldsymbol{u}/c$. Since the rotation axes due to a_μ and $\boldsymbol{d}_\mu$ are orthogonal, the corresponding signals can be separated [42]. In the case of $\boldsymbol{\mu}_\mu$, the anomalous precession period is 2.2 μs, about 300 times the cyclotron period. Assuming that muons are 100% polarized, 1.5×10^{12} positrons have to be detected for a measurement precision of 0.1 ppm [42].

[3] A much higher level of polarization can be obtained by using a magnetic field to align the particle spins [42].

4 An XFEL Based on the Proposed Superconducting Linac

To record the dynamics of atoms requires a probe with Ångstrom (10^{-10} m) wavelength and femtosecond temporal duration (10^{-15} s). Such probes have recently become available with the advent of *X-ray free-electron lasers* (XFELs).[4] The ultrashort pulse duration of an XFEL matches the timescale of non-equilibrium microscopic processes such as electron transfer in molecules, evolution of chemical reactions, vibration dynamics in solid state systems, etc. Nanometer-scale molecular imaging is made possible also by the high degree of *coherence* of the XFEL radiation.

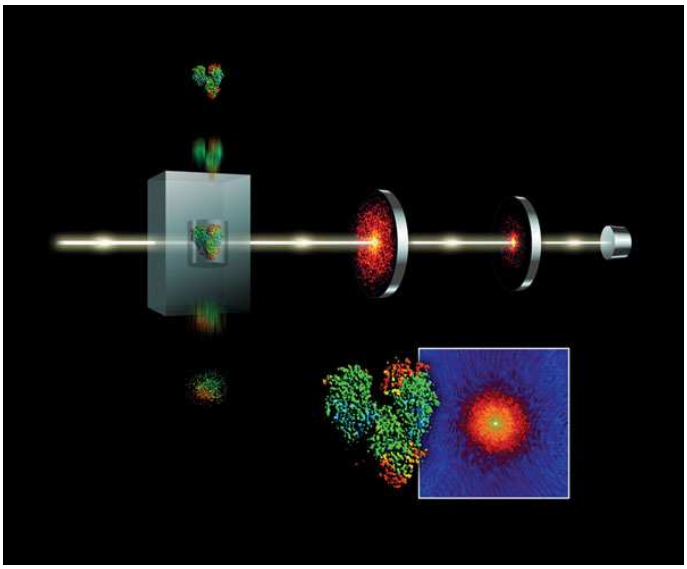

Figure 11: The LCLS records images of protein molecules as they fall through a target chamber. The drawing shows how scattering of X-ray pulses with femtosecond duration records locations of individual atoms before the pulse energy tears the protein apart; credit: LCLS and SLAC.

The peak *spectral brightness* of the two presently most powerful XFEL facilities — LCLS at SLAC (United States) and SACLA at SPring-8 (Japan) — is billion times higher than that of any synchrotron radiation source. Owing to the high intensity of XFEL radiation, laser-irradiated atoms, molecules and atomic clusters can be excited into previously unknown states. Although high-intensity pulses may also destroy molecular structures, they can still be used to produce high-resolution X-ray diffraction patterns (see Fig. 11), from which real-space images of the atomic positions in molecules can be reconstructed. In a typical 'pump-probe' experiment, the evolution of a chemical (or biochemical) reaction, initiated by an optical or IR laser pulse, is observed by a time-delayed X-ray pulse. By varying the delay, such stroboscopic measurements result in femtosecond 'movies' of the evolving system.

4.1 A Simplified Description of X-Ray Free-Electron Lasers

Despite its name, the FEL is more closely related to vacuum tube devices than lasers. Whereas in a conventional laser light amplification is created by the stimulated emission of electrons bound to atoms, the amplification medium of the FEL are 'free' (unbound) electrons. Free-electron lasing is achieved by a single-pass, high-gain FEL amplifier operating in the *self-amplified spontaneous emission* (SASE) mode.

[4]Optical lasers are capable of producing pulses of femtosecond duration, but lack the required spatial resolution. Due to their long pulse durations, X-rays from synchrotron light sources can be used to image atomic structures only in static measurements.

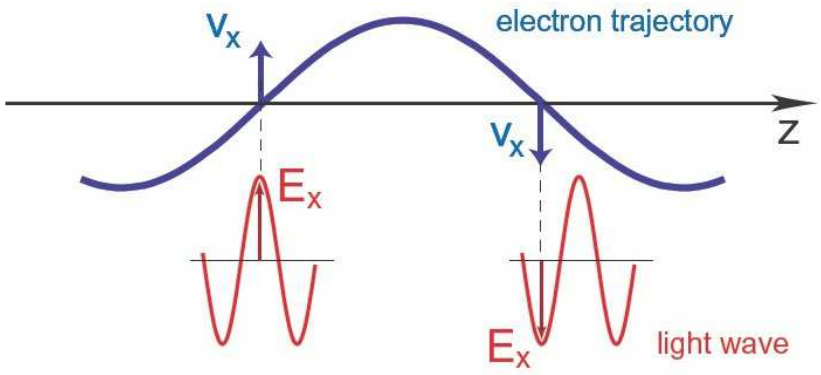

Figure 12: Condition for energy transfer from an electron to the radiation field in an undulator. The electromagnetic wave, which propagates with the speed of light and hence always moves ahead of an electron, has to 'advance' by half an optical wavelength in a half-period of the electron trajectory [43].

An FEL consists of an electron linear accelerator and an *undulator*, a long periodic array of magnets with period λ_u. The undulator generates a sinusoidal transverse magnetic field described by $\mathrm{B} = \mathrm{B}_0 \sin(2\pi z/\lambda_u)$. In the rest frame of an electron, the magnetic field of the undulator becomes a combination of a transverse magnetic field and a transverse electric field, travelling together at almost the speed of light. The electron, therefore, 'sees' the undulator as an electromagnetic wave with wavelength given by the undulator period corrected for the relativistic Lorentz contraction: $\lambda^* = \lambda_u/\gamma$, where the Lorentz factor $\gamma = \mathrm{E}_e/m_e c^2$ is defined as the relativistic energy of the electron in units of its rest energy $m_e c^2$. This wave causes the electron to oscillate as a classical radiating dipole and emit electromagnetic waves with wavelength λ^*.[5] In the laboratory frame, the wavelength of the radiation is Doppler-shifted: $\lambda = \lambda^*\gamma(1 - \beta\cos\theta) \approx (\lambda_u/2\gamma^2)(1 + \gamma^2\theta^2)$, where θ is the angle with respect to the forward direction and $\gamma^2 = (1 - \beta^2)^{-1}$. Taking into account the reduced longitudinal electron velocity caused by the transverse motion (responsible for the second term in Eq. (8)), the *wavelength* of the *first harmonic* of the observed radiation is given by [43, 44]

$$\lambda = \frac{\lambda_u}{2\gamma^2}\left(1 + \frac{K^2}{2} + \gamma^2\theta^2\right) \tag{8}$$

where the dimensionless quantity

$$K = \frac{e\mathrm{B}_0\lambda_u}{2\pi m_e c} = 0.934\,\mathrm{B}_0[\mathrm{Tesla}]\,\lambda_u[\mathrm{cm}] \tag{9}$$

is the undulator *deflection parameter*. Typically, $\lambda_u \approx 3$ cm and $\gamma \approx 10^4$; hence, $\lambda \approx 0.1$ nm.

The optical amplification in an XFEL is caused by a sustained energy transfer from the electrons to the co-moving radiation field. This energy transfer can only take place if the transverse velocity component of an electron and the electric vector of the electromagnetic wave point in the same direction. For this condition to be satisfied, the electromagnetic wave has to 'advance' by the right amount (see Fig. 12), and this is only possible for a certain wavelength λ_ℓ. A simple calculation shows that $\lambda_\ell = \lambda(\theta = 0)$, where $\lambda(\theta)$ is given by Eq. (8).

Initially, an electron bunch in the undulator is much longer than the radiation wavelength, and the electrons are distributed uniformly throughout the bunch. Depending on the relative phase

[5] In the laboratory frame, electrons emit radiation in the forward direction within a narrow cone of opening angle $1/\gamma$. The cone is centred around the instantaneous tangent to the electron trajectory. The direction of the tangent varies along the sinusoidal orbit in an undulator, the maximum angle with respect to the z-axis being $\theta_{\max} \sim K/\gamma$, where $K \propto \mathrm{B}_0\lambda_u$. If $\theta_{\max} \leq 1/\gamma$, the radiation field contributions from various sections of the trajectory overlap in space and interfere with each other. Consequently, the radiation spectrum at $\theta = 0$ is nearly monochromatic, and the *angular width* of the *first harmonic* is $\sigma_\theta \sim 1/\gamma\sqrt{N_u}$, where N_u is the number of undulator periods [43].

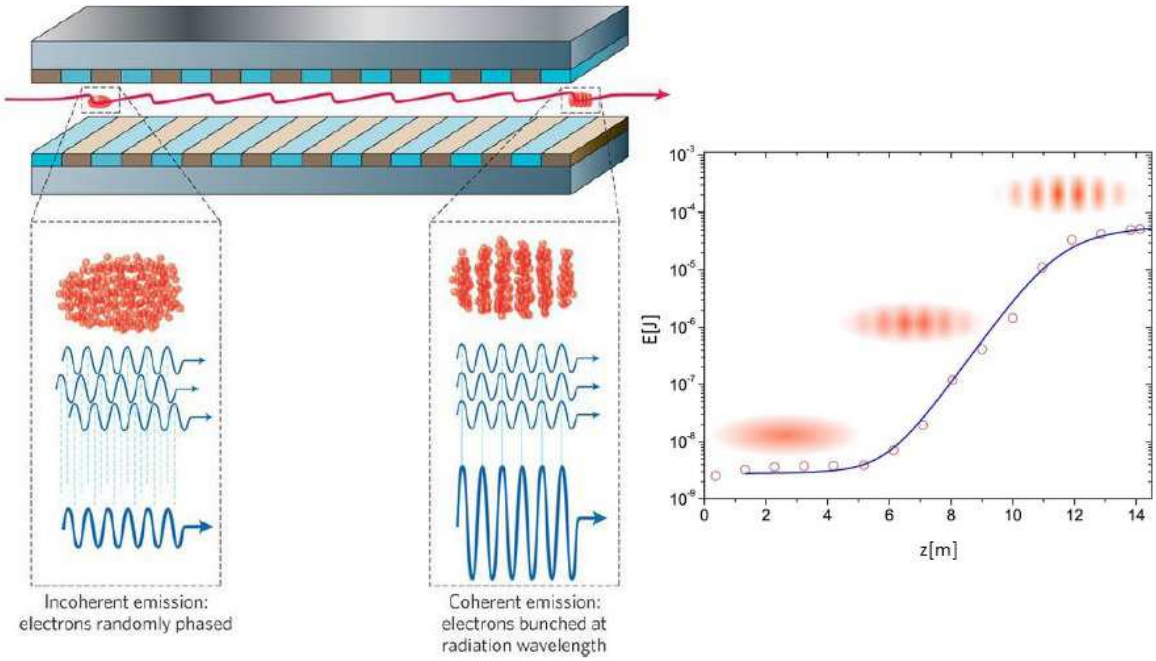

Figure 13: Electrons entering an undulator have random phases and thus initially emit mostly incoherent radiation at the wavelength λ. Since the electrons interact collectively with the radiation they emit, small coherent fluctuations in the radiation field grow and simultaneously begin to bunch the electrons. This collective process continues until the electrons are strongly bunched [45] (left figure). The progress of microbunching and the exponential growth of the FEL pulse energy as a function of the distance z traversed along the undulator are shown in the figure on the right. Open circles represent a measurement [46], and the solid curve is a theoretical prediction [43].

between radiation and electron oscillation, some electrons will gain energy from the radiation field while other electrons will lose energy to the field. As faster electrons catch up with the slower ones, a periodic density modulation on the scale of λ_ℓ (the so-called *microbunching*) begins to develop in the undulator. Since these microbunches are close to the positions where maximum energy transfer to the radiation field takes place, the microbunched electron beam emits coherent radiation at the expense of the beam energy. The increase in the radiation field enhances the microbunching even further, which leads to an *exponential growth* of the FEL pulse energy as a function of the distance z traversed along the undulator: $\mathcal{P}(z) \propto \mathrm{e}^{z/L_\mathrm{g}}$, where $\mathcal{P}$ denotes power and $L_\mathrm{g} \approx 50\lambda_u$ is the *power gain length* (see Fig. 13). The exponential power growth lasts until both the radiation intensity and the electron beam microbunching reach a *saturation level* (at $L_\mathrm{sat} \approx 20L_\mathrm{g}$). This occurs when the beam loses so much energy that the resonant condition is no more satisfied [43].

The total electric field of the undulator radiation is the sum of the fields from all the electrons: $\mathrm{E_{tot}} = \sum_n \mathrm{E}_n \mathrm{e}^{i\phi_n}$, where E_n is the field due to a single electron and ϕ_n is the phase of the electric field from the n^{th} electron. The power emitted by the electrons is given by

$$\mathcal{P} \propto \left| \sum_n \mathrm{E}_n \mathrm{e}^{i\phi_n} \right|^2 = \sum_n \mathrm{E}_n^2 \; + \; \left| \sum_n \sum_m \mathrm{E}_n \mathrm{E}_m \, \mathrm{e}^{i(\phi_n - \phi_m)} \right|_{n \neq m} \tag{10}$$

Since the $N_e \sim 10^7$ electrons within a microbunch oscillate in phase, the individual fields add coherently. In this case ϕ_n is a constant and $|\mathrm{E_{tot}}| \approx n_b N_e \mathrm{E}_0$; here $n_b \sim 10^2$ is the number of microbunches and E_n was set equal to E_0. The dominant contribution to the total *coherently emitted* power comes from the second term in Eq. (10): $\mathcal{P}_\mathrm{coh} \approx n_b (N_e \mathrm{E}_0)^2$. If the radiation is produced by particles oscillating at random phases (*incoherent emission*), the second sum in Eq. (10) tends to interfere destructively (summing the fields is equivalent to a random walk in the complex plane). In this case the dominant first term gives $\mathcal{P}_\mathrm{incoh} \approx n_b N_e \mathrm{E}_0^2 \ll \mathcal{P}_\mathrm{coh}$ [45].

The emission of radiation in an undulator does not occur at one wavelength, but in a *wavelength band* of width $\Delta\lambda$ around the central value given by Eq. (8). Each electron propagating through the undulator emits a wave train consisting of a number of wavelengths equal to the number of undulator periods, N_u. The time duration Δt of this pulse is the *pulse length* $L_p \equiv N_u\lambda$ divided by the speed of light: $\Delta t = N_u\lambda/c$. A pulse of duration Δt has a *frequency bandwidth* $\Delta\nu \sim 1/\Delta t$. Hence, $\Delta\nu \sim c/N_u\lambda = \nu/N_u$, because $\lambda = c/\nu$. Thus,

$$\frac{\Delta\nu}{\nu} = \frac{\Delta\lambda}{\lambda} \sim \frac{1}{N_u} \approx 10^{-3} \tag{11}$$

The wave train is not monochromatic due to its finite length. For typical values $N_u \approx 10^3$ and $\lambda \approx 0.1$ nm, one obtains $\Delta t \approx 0.33$ fs. Since the electrons are distributed throughout a bunch, the *pulse duration* is increased to $\tau_p \sim (\sigma_z/L_p)\Delta t \approx 80$ fs, where $\sigma_z \approx 25$ μm is the *bunch length* and $L_p \approx 0.1$ μm. An 80 fs pulse, therefore, consists of many micropulses of 0.33 fs duration.

The 'shot noise' in an electron beam, the origin of which is the random emission of the electrons from a photocathode (see Fig. 14), causes random fluctuations of the beam density. The radiation produced by such a beam has amplitudes and phases that are random in both space and time. For this reason, SASE X-ray FELs lack *longitudinal* (or *temporal*) *coherence*, characterized by the *coherence length* $L_{\rm coh} \equiv \lambda^2/\Delta\lambda \approx 0.1$ μm. This quantity is defined as the distance of propagation over which radiation with spectral width $\Delta\lambda$ becomes 180° out of phase.[6] The *coherence time*, defined by $t_{\rm coh} \equiv L_{\rm coh}/c \sim 1/\Delta\nu$, is much shorter than the *pulse duration*: $t_{\rm coh} \approx 0.3$ fs.

In order to increase the coherence length in the hard X-ray regime (photons with 0.1 nm wavelength), a '*self-seeding*' method was tested at LCLS [47]. FEL pulses, generated in the first modular section of the LCLS undulator, are spectrally 'purified' by a crystal filter (a diamond monochromator). Since a typical monochromator delays X-rays, the electron bunches exiting the first modular section are appropriately delayed after being diverted around the crystal by a compact magnetic chicane (see Fig. 1 in [47]). The crystal selects a very narrow part of the spectrum, which is further amplified in the second undulator section where the FEL radiation reaches saturation. At LCLS, 'self-seeding' generated X-ray pulses with $\Delta\nu = 0.4$–0.5 eV at $\nu = 8$–9 keV, which represents a factor of 40–50 *bandwidth reduction* with respect to SASE [47].

4.2 The European XFEL as a Prototype of the Proposed X-Ray FEL

The European XFEL, currently under construction at DESY (Germany), is a free-electron laser (FEL) based on self-amplified spontaneous emission (SASE) in the X-ray regime. The FEL consists of a 17.5 GeV superconducting electron linear accelerator and a set of undulators (see Fig. 14) that can generate both SASE FEL X-rays and incoherent radiation. A superconducting linac may accelerate 10 'bunch trains' per second, each train consisting of up to 2700 electron bunches. This results in 27 000 ultrashort X-ray flashes per second — many more than at any other existing XFEL facility. The higher the number of electron bunches, the more scientific instruments can be operated simultaneously. The European XFEL facility will generate ultra-short pulses (≤ 100 fs) of spatially and temporally coherent X-rays with wavelengths in the range $\sim$0.1–5 nm.

The *spectral brightness* (or *brilliance*), $\mathfrak{B}$, of a radiation field is defined as the number of photons per unit phase-space volume per unit fractional bandwidth per unit time. In practical units, $\mathfrak{B}$ can be expressed as

$$\text{Spectral brightness} \equiv \frac{\text{Number of photons}}{(\text{second})(\text{mm}^2)(\text{mrad}^2)(0.1\%\ \text{BW})} \tag{12}$$

where BW denotes *spectral bandwidth*. The quantity $\mathfrak{B}$ determines how much monochromatic radiation can be focused onto a tiny spot on the target. The *peak spectral brightness* of the FEL

[6] For a wavelength λ propagating through n cycles, $L_{\rm coh} = n\lambda$; for a wavelength $\lambda + \Delta\lambda$ propagating through $(n - 1/2)$ cycles, $L_{\rm coh} = (n - 1/2)(\lambda + \Delta\lambda)$. Hence $L_{\rm coh} \approx \lambda^2/2\Delta\lambda$, although $L_{\rm coh} \equiv \lambda^2/\Delta\lambda$ is also often used.

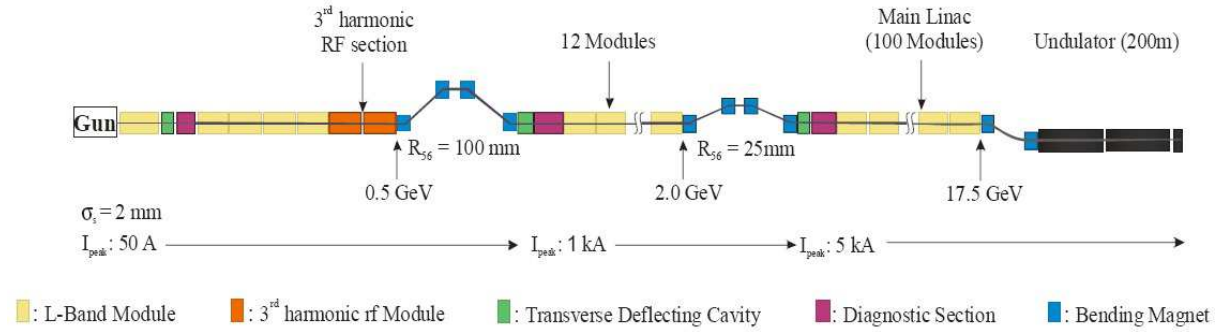

Figure 14: Schematic layout of the European XFEL [48]. Electron bunches, each with a charge of 1 nC, are extracted from a photocathode by short ultraviolet laser pulses and then focused and accelerated inside a radio-frequency cavity ('RF gun') to an energy of 120 MeV. In order to produce 5 kA peak currents necessary for lasing, the bunches are further accelerated and longitudinally compressed down to 25 μm using two magnetic chicanes (at 0.5 and 2.0 GeV). After traversing the main linac, where their energy is increased to 17.5 GeV, the bunches enter FEL undulators.

is the brightness measured during the very short duration of an FEL pulse. The peak brilliance of the European XFEL is expected to be 5×10^{33} photons/second/mm^2/mrad^2/0.1% BW.

As mentioned earlier, the coherent superposition of the radiation fields from *all* microbunches is responsible for the nearly monochromatic spectrum and small divergence of the radiation emitted in the forward direction (see footnote 5 and [43]). Recall also that 'self-seeding' can substantially improve longitudinal (temporal) coherence of SASE XFEL radiation (see Section 4.1). Thus, the radiation from an X-ray FEL has a narrow bandwidth, is transversely and longitudinally coherent, and is fully polarized. The coherently emitted XFEL spectral lines appear in addition to the spontaneously emitted undulator spectrum that extends into the MeV energy region (see Fig. 15).

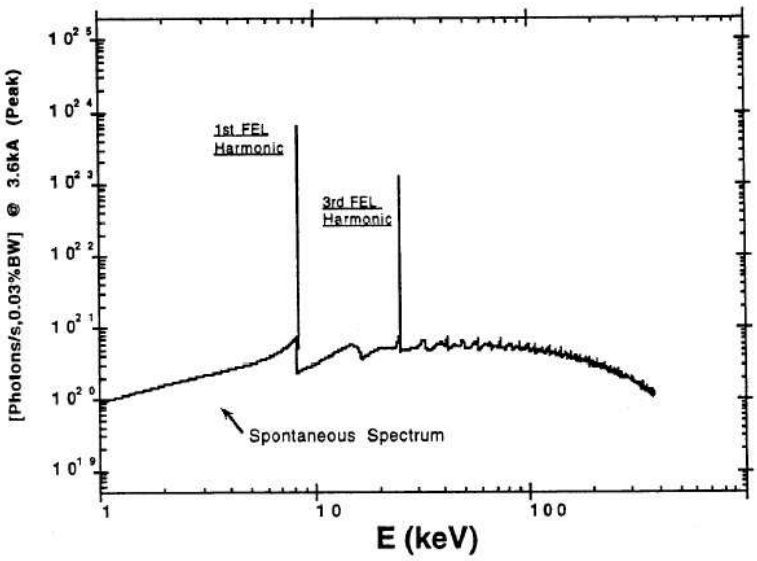

Figure 15: Computed spectral flux of spontaneous undulator and FEL radiation at LCLS. Plotted is the number of photons per second and 0.3% bandwidth as a function of photon energy [49].

The micropulses that form an FEL pulse give rise to 'spikes' shown in Fig. 16. The amplitudes of the micropulses vary greatly as a consequence of the amplified stochastic variations in the electron density. Within a micropulse, the radiation is both transversely and longitudinally coherent. The duration of a micropulse is roughly $t_{\rm coh}$, the *coherence time*. In the SASE 1 and SASE 2 undulators at the European XFEL, $t_{\rm coh} = 0.2$–0.38 fs [48]. The number of 'spikes' in a pulse is given by the ratio of the *bunch length* to the *coherence length*: $\sigma_z/L_{\rm coh} = (25\ \mu{\rm m})/(0.1\ \mu{\rm m}) \approx 250$.

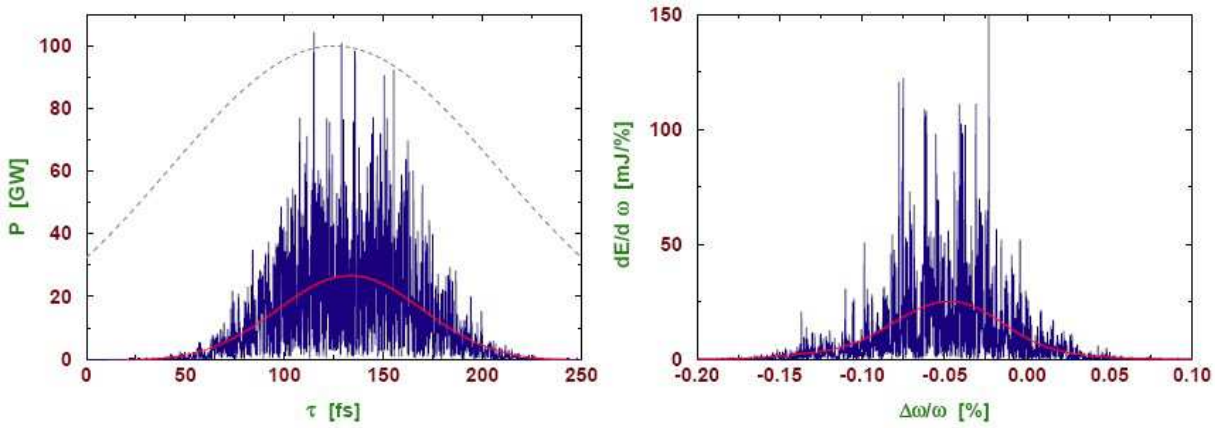

Figure 16: Typical temporal (left) and spectral (right) structure of the radiation pulse from a SASE XFEL at a wavelength of 0.1 nm [50]. The red lines correspond to average values. The dashed line represents the axial density profile of the electron bunch. The line width is inversely proportional to the coherence time.

The spectrum of undulator radiation is sharply peaked around *odd harmonics*[7] (see Fig. 15). The photon energy that corresponds to the n^{th} harmonic is given by

$$\mathrm{E}_n\,[\mathrm{keV}] \;=\; 0.9496\,\frac{n\mathrm{E}_e^2\,[\mathrm{GeV}]}{\lambda_u\,[\mathrm{cm}](1+K^2/2+\gamma^2\theta^2)} \tag{13}$$

where E_e is the electron beam energy and θ is the radiation detection angle (with respect to the forward direction). For $\theta = 0$ and the SASE 2 undulator parameters $\lambda_u = 4.8$ cm and $K = 6.1$, for example, Eq. (13) yields $\mathrm{E}_1 = 12.2$ keV [48].

At the exit of the SASE 1 undulator, the photon beam divergence is $\sigma_\theta \sim 1/\gamma\sqrt{N_u} \approx 1\,\mu$rad (see footnote 5) and the beam size is $70\,\mu\mathrm{m} \times 70\,\mu\mathrm{m}$, the diameter of a fine needle. This beam can be focused to an area of $0.1\,\mu\mathrm{m} \times 0.1\,\mu\mathrm{m}$ (the size of a virus) at an experimental station located a couple of hundred meters from the undulator exit [51]. Through variable focusing, the flux density of an XFEL beam can therefore be tuned by a factor of about one million. The SASE 1 undulator will deliver 10^{12} photons in an ultra-short pulse of 100 fs duration (the timescale of molecular vibrations), yielding a peak power of about 20 GW at a photon energy $\mathrm{E} \approx 12$ KeV ($\lambda = hc/\mathrm{E} \approx 0.1$ nm).

As already mentioned, nanometre-scale molecular imaging is made possible by the high degree of coherence of the XFEL radiation. The coherence quality of a light source is best described by the *degeneracy parameter* $\mathfrak{D}$, defined as the number of photons per coherent phase-space volume $(\lambda/2)^2$ per coherence time $c^{-1}(\lambda^2/\Delta\lambda)$. Since the unit fractional bandwidth is $\Delta\lambda/\lambda$,

$$\mathfrak{D} \equiv \mathfrak{B}\left(\frac{\lambda}{2}\right)^2\left(\frac{\lambda^2/\Delta\lambda}{c}\right)\left(\frac{\Delta\lambda}{\lambda}\right) = \frac{\mathfrak{B}\lambda^3}{4c} \approx 8.3\times10^{-25}\,\mathfrak{B}\lambda^3 \tag{14}$$

Here $\mathfrak{B}$ is the *brilliance* and $\lambda\,[0.1\,\mathrm{nm}]$ the wavelength of the source. Recall that all photons in a single micropulse are completely coherent. Since each pulse contains $\sim 10^{12}$ photons and a few hundred micropulses, there are 10^9 indistinguishable ('degenerate') photons in the coherence volume. In comparison, $\mathfrak{D} \approx 0.03$ at a synchrotron source with $\lambda = 0.1$ nm. Because of the large transverse coherence area of $70 \times 70\,\mu\mathrm{m}^2$ and the large number of coherent photons per pulse, an interference ('speckle') pattern can be recorded with a single XFEL pulse [52, 53].

[7] The occurrence of *higher harmonics* is explained in [43]. In the forward region ($\theta = 0$) of a planar undulator, only the odd higher harmonics are observed, while the off-axis radiation contains also the even harmonics. For the European XFEL, simulations predict that the relative contribution to the total radiation power of the 3^{rd} and the 5^{th} harmonic is about 1% and 0.03%, respectively [48].

5 Summary and Acknowledgements

The main 'bottleneck' limiting the beam power in circular machines is caused by space charge effects that produce beam instabilities. Such a 'bottleneck' exists at the J-PARC proton synchrotron complex, and is also intrinsic to the 'proton drivers' envisaged at CERN and Fermilab. In order to maximally increase the beam power of a 'proton driver', it is proposed to build a facility consisting solely of a low-energy injector linac (PI) and a high-energy *pulsed* superconducting linac (SCL). The 2.5 GeV PI would serve both as an injector to the SCL and a source of proton beams that could be used to copiously produce neutrons and muons. Protons accelerated by the SCL to 20 GeV would be transferred through the KEK Tristan ring in order to create neutrino, kaon and muon beams for fixed-target experiments. At a later stage, a 70 GeV proton synchrotron could be installed inside the Tristan ring. The proposed facility would be constructed using the existing KEK accelerator infrastructure.

High-power proton linear accelerators have a wide range of applications including spallation neutron sources, nuclear waste transmutation, production of radioisotopes for medical use, etc. A number of laboratories worldwide have expressed interest in building 'proton drivers' that would primarily deliver high-intensity neutrino, kaon and muon beams.

Experiments with high-intensity neutrino beams are designed primarily to explore the mass spectrum of the neutrinos and their properties under the CP symmetry. The proposed T2HK (Tokai-to-Hyper-Kamiokande) project, for example, is a natural extension of the successful T2K (Tokai-to-Super-Kamiokande) long-baseline neutrino oscillation experiment. Hyper-Kamiokande (HK), a water Cherenkov detector with a fiducial mass of 0.54 million metric tons, would serve as a 'far' detector for neutrino beams produced at J-PARC, situated 295 km away from Kamioka.

In case HK *is never built, the proposed* '*proton driver*' *and the existing* Super-Kamiokande *detector would produce, within a given period of time, roughly the same number of* ν_e *and* $\bar{\nu}_e$ '*appearance events*' *as the* T2HK *experiment.* Alternatively, a 100 kiloton water Cherenkov detector could be built at Okinoshima, located along the T2K beamline at a distance of about 650 km from KEK. Using the proposed 'proton driver', the detector at Okinoshima and Super-Kamiokande, one could determine the neutrino mass hierarchy as well as measure the CP-violating phase in the neutrino mixing matrix. To produce neutrino beams, a DC magnetic horn would be employed.

Some of the most important discoveries in particle physics emerged from high-precision studies of K mesons ('kaons'), in particular *neutral kaons*. A deeper insight into CP violation is expected to be gained from measurements of ultra-rare kaon decays such as $K_{\rm L}^0 \to \pi^0\nu\bar{\nu}$ and $K_{\rm L}^+ \to \pi^+\nu\bar{\nu}$. These decays provide important information on higher-order effects in electroweak interactions, and therefore can serve as a probe of new phenomena not predicted by the Standard Model.

A unique feature of the proposed facility is the use of superconducting ILC-type cavities to accelerate *both* protons and electrons, which considerably increases its physics potential. Polarized electrons and positrons can be employed to study the structure of composite particles and the dynamics of strong interactions, as well as to search for new physics beyond the Standard Model.

An SCL-based X-ray free-electron laser (XFEL) and a synchrotron light source for applications in materials science and medicine are also envisaged. The ultrashort pulse duration of an XFEL matches the timescale of non-equilibrium microscopic processes, allowing the dynamics of atoms and molecules to be recorded in the form of femtosecond 'movies'.

Acknowledgements

For many useful discussions regarding various aspects of this proposal, I am very grateful to K. Fujii, K. Hagiwara, T. Higo, E. Kako, Y. Kamiya, K. Oide, K. Takayama and K. Tokoshuku. I wish to express my special gratitude to Kaoru Yokoya for the invaluable help and encouragement I have received from him over the years.

References

[1] G. Aad et al. (Atlas Collab.), Phys. Lett. B716, 1 (2012).

[2] S. Chatrchyan et al. (CMS Collab.), Phys. Lett. B716, 30 (2012).

[3] J. Beringer et al. (Particle Data Group), Phys. Rev. D86, 010001 (2012) and 2013 update for the 2014 edition.

[4] A. Yano et al., *The Toshiba* E3736 *Multi-Beam Klystron*, Proc. LINAC 2004, Lübeck, Germany (2004).

[5] E. Gelvich et al., IEEE Trans. Microwave Theory Tech. 41(1), pp 15–19 (1993).

[6] A. Yamamoto, IEEE Trans. Appl. Supercond. Vol. 19, No. 3, pp 1387–1393 (2009); T. Saeki et al., Proc. IPAC 2013, Shangai, China (2013).

[7] D. Faircloth, *Ion sources for high-power hadron accelerators*, arXiv:1302.3745 (2013).

[8] I. M. Kapchinsky and V. A. Tepliakov, Prib. Tekh. Eksp. 2, pp 19-22 (1970).

[9] M. Vretenar, *Low-beta structures*, CERN Yellow Report 2011-007, pp 319–340 (2011); arXiv:1201.2593 (2012).

[10] M. Lindroos et al., Proc. LINAC 2012, Tel Aviv, Israel (2012).

[11] A. Mosnier, *A survey of high-power proton linacs*, Proc. LINAC 2002, Gyeongju, Korea (2002).

[12] R. Garoby et al., *Proton drivers for neutrino beams and other high intensity applications*, Journal Phys. Conf. Series 408, 012016 (2013).

[13] E. Baussan et al., Nucl. Phys. B 885, 127–149 (2014); arXiv:1309.7022v3 (2013).

[14] U. Al-Binni et al., *Project X, Physics Opportunities*, arXiv:1306.5009v2 (2013).

[15] J. Dudek et al. (JLab), *Physics Opportunities with the 12 GeV Upgrade at Jefferson Lab*, arXiv:1208.1244v2 (2012).

[16] E. Voutier, *Physics Perspectives at JLab with a Polarized Positron Beam*, arXiv:1402.2814v1 (2014).

[17] R. Belusevic, *Relativity, Astrophysics and Cosmology*, Wiley-VCH Verlag, Weinheim 2008.

[18] M. Shaposhnikov, Prog. Theor. Phys. 122, pp 185–2013 (2009).

[19] K. Abe et al., *Letter of Intent: The Hyper-Kamiokande Experiment*, arXiv:1109.3262v1 (2011).

[20] R. N. Cahn et al., *White Paper: Measuring the Neutrino Mass Hierarchy*, arXiv:1307.5487v2 (2013).

[21] K. Hagiwara et al., KEK-TH-1568; arXiv:1209.2763v1 (2012).

[22] J. Back et al., Phys. Rev. Spec. Topics — Accelerators and Beams 16, 021001 (2013).

[23] K. T. Mc Donald et al., in *Proc. First International Particle Accelerator Conf.*, Kyoto, Japan (2010).

[24] E. Baussan et al., Journal of Phys. Conf. Series 408, 012061 (2013).

[25] Y. Kamiya, KEK, private communication.

[26] T. Omori et al., Phys. Rev. Lett. 96, 114801 (2006).

[27] J. Grames et al., Jlab Experiment E12-11-105 (2011).

[28] . Y. B. Zeldovich, Zh. Eksp. Teor. Fiz. 36, pp 964-966 (1959).

[29] E. Derman and W. J. Marciano, Annals Phys. 121, 147 (1979).

[30] A. Czarnecki and W. J. Marciano, Phys. Rev. D 53, pp 1066–1072 (1996).

[31] J. Mammei (MOLLER Collaboration), Nuovo Cim. C 35. pp 203–208 (2012).

[32] K. S. Kumar et al., Ann. Rev. Nucl. Sci. 63, pp 237–267 (2013).

[33] R. Belusevic, *Neutral Kaons*, Springer-Verlag, Berlin 1999.

[34] J. Brod, M. Gorbahn and E. Stamou, Phys. Rev. D 83, 034030 (2011).

[35] A. Belyaev et al., CERN-TH/2001-175; arXiv:hep-ph/0107046v2 (2001).

[36] A. Buras, *CP Violation and Rare Decays of K and B Mesons*, arXiv:hep-ph/9905437 (1999).

[37] T. Yamanaka (KOTO Collaboration), Prog. Theor. Exp. Phys. 2012, 02B006 (2012).

[38] A. Artamonov et al., Phys. Rev. D 79, 092004 (2009).

[39] J. L. Ritchie (ORKA Collaboration), arXiv:1301.0335 (2013).

[40] NA62 *Status Report to the* CERN SPSC, CERN-SPSC-2014-009 (2014).

[41] J. Miller, E. de Rafael and B. L. Roberts, Rep. Prog. Phys. 70, pp 795–881 (2007).

[42] M. Aoki et al., KEK-J-PARC-PAC2009-12 (2009); T. Mibe, Chinese Phys. C 34(6), pp 745–748 (2010).

[43] P. Schmüser, M. Dohlus and J. Rossbach, *Ultraviolet and Soft X-Ray Free-Electron Lasers*, Springer-Verlag, Berlin (2008).

[44] Zh. Huang and K. Kim, Phys. Rev. Spec. Topics — Accelerators and Beams 10, 034801 (2007).

[45] B. McNeil and N. Thompson, Nature Photonics 4, pp 814–821 (2010).

[46] http://flash.desy.de/sites2009/site_vuvfel/content/e395e2188/FLASH-Broschrefrs_web.pdf

[47] J. Amann et al., Nature Photonics 6, pp 693–698 (2012).

[48] R. Abela et al., *The European X-Ray Free-Electron Laser, Technical Design Report*, DESY 2006-097 (2007).

[49] J. Arthur, SLAC-PUB-8276 (1999).

[50] M. Abd-Elmeguid, TESLA *Technical Design Report* Part V, (2001).

[51] I. Agapov et al., Proc. FEL2014, Basel, Switzerland (2014).

[52] C. Pellegrini and J. Stöhr, *X-Ray Free-Electron Lasers — Princiles, Properties and Applications*, Nucl. Instrum. Meth. A 500, 33–40 (2003).

[53] A. Barty, J. Phys. B, Atom. Mol. Opt. Phys. 43, 194014 (2010).